

Research Article

Adaptive Image Restoration via a Relaxed Regularization of Mean Curvature

Mingxi Ma,¹ Jun Zhang ,^{1,2} Chengzhi Deng,¹ Zhaoyang Liu,¹ and Yuanyun Wang¹

¹Jiangxi Province Key Laboratory of Water Information Cooperative Sensing and Intelligent Processing, Nanchang Institute of Technology, Nanchang 330099, Jiangxi, China

²College of Electrical and Information Engineering, Hunan University, Changsha 410082, Hunan, China

Correspondence should be addressed to Jun Zhang; junzhang0805@126.com

Received 22 July 2020; Revised 29 October 2020; Accepted 3 November 2020; Published 1 December 2020

Academic Editor: S. A. Edalatpanah; saedalatpanah@gmail.com

Copyright © 2020 Mingxi Ma et al. This is an open access article distributed under the Creative Commons Attribution License, which permits unrestricted use, distribution, and reproduction in any medium, provided the original work is properly cited.

In this paper, a new relaxation model based on mean curvature for adaptive image restoration is proposed. To solve the problem efficiently, an alternating direction method of multipliers (ADMMs) is proposed. Furthermore, a rigorous convergence theory of the proposed algorithm is established. We also give the complexity analysis of our proposed method. Experimental results are provided to demonstrate the effectiveness and efficiency of the proposed method over a state-of-the-art method on synthetic and natural images.

1. Introduction

Image restoration has always been a research hotspot in the field of image processing. To solve this inverse problem, one of the most popular research directions is applying variational regularization methods. It mainly includes total variation (TV) regularization [1–3], nonlocal regularization [4], sparse regularization [5], higher-order regularization based on higher-order derivatives [6–9], and fractional-order regularization based on fractional-order derivatives [10, 11].

As a classic regularization method, TV regularization has been successfully applied to image restoration, image segmentation, image reconstruction, image decomposition, and phase recovery. When using it for image denoising, the edge-preserving effect is better. For the TV-based image denoising problem, researchers have proposed a variety of fast and efficient numerical algorithms, such as dual algorithm [12], primal-dual algorithm [13], split Bregman method [14], augmented Lagrangian method [15, 16], alternating direction method of multipliers (ADMMs) [17], proximity

algorithm [18], domain decomposition method [19], and nonlinear multigrid method [3]. However, after denoising with TV regularization, the image often exhibits staircase effects in the flat area. Second, this type of regularization model will cause image contrast loss.

To reduce the staircase effects, a number of higher-order models have been developed [20, 21]. Among them, let us specially note the mean curvature model [9, 22] and Euler's elastica model [23–27], which are nonconvex so that the numerical algorithms converge to the local optimal solution. The mean curvature-based image denoising model (called the MC model) can be formulated as follows:

$$\min_u \int_{\Omega} \left| \nabla \cdot \left(\frac{\nabla u}{\sqrt{1 + |\nabla u|^2}} \right) \right| dx dy + \frac{1}{2\lambda} \int_{\Omega} (u - f)^2 dx dy, \quad (1)$$

where u and f represent the restored image and the noisy image, ∇ is the gradient operator, the weighting parameter $\lambda > 0$ controls the amount of denoising, and

$\nabla \cdot (\nabla u / \sqrt{1 + |\nabla u|^2})$ is the mean curvature of the image surface $\phi(x, y, z) = u(x, y) - z = 0$. As mentioned in [28], the MC model preserves image contrast better for cleaned images than the TV model. In addition, this model handles corners better for synthetic images than the TV and Euler's elastica models. In view of a number of valuable properties of the MC model, designing fast iterative algorithms for its solution has important theoretical and practical significance. There are some different augmented Lagrangian methods for solving the MC model. In [28], original unconstrained problem (1) was transformed into a constrained optimization problem and the saddle-points of the corresponding augmented Lagrangian functional are obtained from solving several subproblems alternatively. Some subproblems had closed form solutions while others were solved by fast Fourier transform (FFT). Subsequently, in [29], the solutions of two subproblems were obtained by a Gauss-Seidel method. In addition to the reduction of computational cost, this approach can be applied to computational domains with nonperiodic boundaries. Besides, a fast linearized augmented Lagrangian method was proposed to further improve the convergence rates [30]. In this method, all subproblems have closed form solutions. However, due to the nonconvexity of the MC model, it is still very hard to find suitable model parameter and penalization parameters.

By choosing the regularization parameter based on the inverse gradient, in [31], Thanh et al. proposed some adaptive image restoration methods. Besides, in [32, 33], the authors proposed the adaptive TV^p regularization and the adaptive weighted TV^p regularization for image denoising, respectively. In [34], a novel adaptive image denoising method was proposed, which combines a Tchebichef moment-based sparse regularizer with an adaptive steerable total variation regularizer.

By minimizing the L^1 norm of the gradient of the unit normal, Duan et al. proposed a novel variational model as follows [8]:

$$\min_u \int_{\Omega} \left| \nabla \left(\frac{\nabla u}{\sqrt{1 + |\nabla u|^2}} \right) \right| dx dy + \frac{1}{2\lambda} \int_{\Omega} (u - f)^2 dx dy, \quad (2)$$

and proved this model with the ability to preserve image contrast and sharp edges during denoising. Due to the high nonlinearity and nonconvexity of its regularization term, the relaxation form of model (2) was studied. Namely, they proposed a spatially adaptive hybrid regularization-based minimization problem, which can be given as

$$\min_u \int_{\Omega} \alpha(x, y) |\nabla u| + \beta(x, y) |\nabla^2 u| dx dy + \frac{1}{2\lambda} \int_{\Omega} (u - f)^2 dx dy, \quad (3)$$

where operator ∇^2 represents the second-order gradient, $\alpha(x, y) = |\nabla 1 / \sqrt{1 + |\nabla u|^2}|$ and $\beta(x, y) = (1 / \sqrt{1 + |\nabla u|^2})$. For solving this relaxation model, the ADMM-based numerical algorithm was presented and its convergence was

proved [8, 35]. ADMM is a fast method for solving many regularization problems. It has been widely applied in many fields, such as hyperspectral image unmixing [36], classification [37], and fusion [38].

Inspired by the successful application of the relaxation technique, in this paper, we present a new form for the MC model (1) and propose its relaxation model. Moreover, we propose an efficient ADMM with guaranteed convergence. Compared with the ADMM-based algorithm for solving model (3), our method is faster.

The organization of the paper is as follows: In Section 2, the new form of the MC model (1) is presented, and then its geometric properties and its relaxation form together with connections to the existing models are introduced. Section 3 details an efficient ADMM for solving the proposed relaxation model. The convergence and complexity of the proposed algorithm are also studied in this section. Experimental results on synthetic and natural images are presented in Section 4 to show the effectiveness and efficiency of our proposed method. Finally, Section 5 concludes the paper.

2. Adaptive TV and Laplacian Regularization Model

In this section, we first give a new form for the MC model (1). Then, we introduce its geometric properties for image denoising. Finally, we propose a relaxation version using a spatially adaptive TV and Laplacian regularization and analyze the connections to the existing models.

2.1. New Form for the MC Model. Let us first review the MC model.

For a given image $f: \Omega \rightarrow \mathbb{R}$ where $\Omega \subset \mathbb{R}^2$ is the image domain, the corresponding image surface is $(x, y, f(x, y))$ or $z = f(x, y)$. The aim of denoising is to find a piecewise smooth surface $z = u(x, y)$ to approximate it. Meanwhile, we would like to preserve the geometric features, such as edges of objects and corners. We also expect to preserve image contrasts. To this end, the L^1 norm of mean curvature of the image surface was used in [9]. In the following, to introduce the mean curvature of surface $z = u(x, y)$, a level set function $\phi(x, y, z) = u(x, y) - z$ is considered. Obviously, its zero level set corresponds to the surface. Then, the mean curvature of this surface can be defined as

$$H_u = \nabla \cdot \left(\frac{\nabla \phi}{|\nabla \phi|} \right) = \nabla \cdot \left(\frac{\nabla u}{\sqrt{1 + |\nabla u|^2}} \right). \quad (4)$$

Using the L^1 norm of mean curvature as a regularization term, the MC model was proposed as follows:

$$\min_u \int_{\Omega} \left| \nabla \cdot \frac{\nabla u}{\sqrt{1 + |\nabla u|^2}} \right| dx dy + \frac{1}{2\lambda} \int_{\Omega} (u - f)^2 dx dy. \quad (5)$$

Since

$$\nabla \cdot \left(\frac{\nabla u}{\sqrt{1 + |\nabla u|^2}} \right) = \nabla u \cdot \nabla \frac{1}{\sqrt{1 + |\nabla u|^2}} + \frac{1}{\sqrt{1 + |\nabla u|^2}} \Delta u, \quad (6)$$

we can obtain a new form of the MC model which is

$$\min_u \int_{\Omega} \left| \nabla u \cdot \nabla \frac{1}{\sqrt{1 + |\nabla u|^2}} + \frac{1}{\sqrt{1 + |\nabla u|^2}} \Delta u \right| dx dy + \frac{1}{2\lambda} \int_{\Omega} (u - f)^2 dx dy. \quad (7)$$

Because this model is nonconvex, high order, and highly nonlinear, its complete study is nontrivial. However, one can get some insight into its features.

2.2. Features of Model (7). In this subsection, the features of model (7) will be introduced. One can refer to [9] for more details.

If $|\nabla u| \ll 1$ and $|\Delta u| \ll 1$ for each point in a region, the evolution equation corresponding to the gradient descent flow of model (7) behaves like the biharmonic heat equation in that region. Owing to the property that the biharmonic heat equation can damp high frequency signals quickly, model (7) can remove noise efficiently.

In order to illustrate why model (7) can preserve image contrasts, one may consider a simple image $f = h_{\chi_{B(0,R)}}(x, y)$ defined on $\Omega = (-2R, 2R) \times (-2R, 2R)$ with $\chi_{B(0,R)}$ being the characteristic function, $B(0, R)$ being an open disk in \mathbb{R}^2 centered at the origin with radius R , and $h > 0$. Since f is radial symmetric, and one can approximate it by a sequence of smooth radial symmetric function g_n . Referring to [9], the properties of preserving image contrasts and sharp edges about model (7) are guaranteed by the following lemma and theorem:

Lemma 1. *Assuming that $f = h_{\chi_{B(0,R)}}(x, y)$ is an image defined as above, we have*

$$\int_{\Omega} |H_f| dx dy = 4\pi R, \quad (8)$$

where $H_f = \nabla f \cdot \nabla (1/\sqrt{1 + |\nabla f|^2}) + (\sqrt{1 + |\nabla f|^2}) \Delta f$.

The integral indicates that the regularizer of model (7) does not rely on heights of signals. With the conclusion of this lemma, one can further obtain the following theorem:

Theorem 1. *Let $f = h_{\chi_{B(0,R)}}(x, y)$ be an image defined as above. Then, there exists a constant $C > 0$ such that if $\lambda < C$, f is a minimizer of model (7).*

This theorem demonstrates that model (7) is able to preserve image contrasts, once λ is chosen to be small enough. In contrast, a loss of image contrast may appear while using the ROF model, for whatever small λ . Besides, this theorem illustrates that the model can keep sharp edges as the ROF model.

To illustrate why the model can preserve object corners, one needs to consider a different image $f = h_{\chi_E}$ defined on $\Omega = (-R, R) \times (-R, R)$ with $E = (0, R) \times (0, R)$ [9]. Similar results are presented in the following lemma and theorem:

Lemma 2. *Let $f = h_{\chi_E}$ be an image defined on a rectangle $\Omega = (-R, R) \times (-R, R)$ with $E = (0, R) \times (0, R)$. Then,*

$$\int_{\Omega} |H_f| dx dy = 4R. \quad (9)$$

Theorem 2. *Let $f = h_{\chi_E}$ be defined as the above lemma, then there exists a constant $C > 0$ such that if $\lambda < C$, f is a minimizer of model (7).*

Theorem 2 indicates another key feature of model (7) on preserving object edges once λ is small enough.

2.3. Proposed Relaxation Model and Connections to the Previous Models. Although the new form of the MC model has good properties in preserving image contrasts, sharp edges, and object corners, it is still nonconvex and highly nonlinear. Motivated by the success of relaxation in [8], by relaxing the regularization term, we reformulate (7) into a spatially adaptive TV and Laplacian regularization model, which can be expressed as

$$\min_u \int_{\Omega} (\alpha(x, y)|\nabla u| + \beta(x, y)|\Delta u|) dx dy + \frac{1}{2\lambda} \int_{\Omega} (u - f)^2 dx dy, \quad (10)$$

where

$$\alpha(x, y) = \left| \nabla \frac{1}{\sqrt{1 + |\nabla u|^2}} \right|, \quad (11)$$

$$\beta(x, y) = \frac{1}{\sqrt{1 + |\nabla u|^2}}.$$

It is straightforward to see that model (10) is just the relaxation version of the MC model (1). In [39], an effective model which combines the total variation with the Laplacian regularizer (TVL) was introduced:

$$\min_u \mu_1 \|\nabla u\|_1 + \mu_2 \|\Delta u\|_1 + \frac{1}{2} \|KAu - d\|_2^2, \quad (12)$$

where K and A represent the blurring operator and the Abel transform, respectively. μ_1 and μ_2 are two constants. The regularization of our model (10) can be seen as an adaptive form of this TVL regularization. Replacing Δ in (10) by ∇^2 , it becomes the spatially adaptive first- and second-order regularization model (3) proposed in [8]. Compared with the isotropic model, the corresponding anisotropic model is faster when it achieves almost the same denoising effect. Therefore, in order to improve the computational complexity, it is reasonable to use the Laplacian operator Δ to replace the isotropic second-order gradient operator ∇^2 .

3. The Proposed Algorithm

In this section, we propose an efficient numerical algorithm based on the popular ADMM for solving the proposed model (10). Besides, we analyze its convergence and complexity.

3.1. *Algorithm Description.* Firstly, we introduce two auxiliary variables \mathbf{p} and q to reformulate (10) as follows:

$$\min_{u, \mathbf{p}, q} \int_{\Omega} (\alpha(x, y)|\mathbf{p}| + \beta(x, y)|q|) dx dy + \frac{1}{2\lambda} \int_{\Omega} (u - f)^2 dx dy,$$

$$\text{s.t. } \mathbf{p} = \nabla u, q = \Delta u.$$

(13)

The augmented Lagrangian functional corresponding to (13) is

$$\begin{aligned} \mathcal{L}(u, \mathbf{p}, q; \lambda_1, \lambda_2) = & \int_{\Omega} (\alpha(x, y)|\mathbf{p}| + \beta(x, y)|q|) dx dy + \frac{1}{2\lambda} \int_{\Omega} (u - f)^2 dx dy, \\ & + \int_{\Omega} \lambda_1 \cdot (\mathbf{p} - \nabla u) dx dy + \frac{r_1}{2} \int_{\Omega} (\mathbf{p} - \nabla u)^2 dx dy, \\ & + \int_{\Omega} \lambda_2 (q - \Delta u) dx dy + \frac{r_2}{2} \int_{\Omega} (q - \Delta u)^2 dx dy, \end{aligned} \quad (14)$$

where λ_1 and λ_2 are Lagrangian multipliers and r_1 and r_2 are positive penalty parameters. By applying the ADMM, one needs to minimize three subproblems with other variables

fixed and update two Lagrangian multipliers at each iteration which is

$$\left\{ \begin{aligned} u^{k+1} &= \arg \min_u \frac{1}{2\lambda} \int_{\Omega} (u - f)^2 dx dy + \frac{r_1}{2} \int_{\Omega} \left(\mathbf{p}^k - \nabla u + \frac{\lambda_1^k}{r_1} \right)^2 dx dy + \frac{r_2}{2} \int_{\Omega} \left(q^k - \Delta u + \frac{\lambda_2^k}{r_2} \right)^2 dx dy + \frac{\delta_1}{2} \int_{\Omega} (u - u^k)^2 dx dy, \\ \mathbf{p}^{k+1} &= \arg \min_{\mathbf{p}} \int_{\Omega} \alpha^{k+1}(x, y) |\mathbf{p}| dx dy + \frac{r_1}{2} \int_{\Omega} \left(\mathbf{p} - \nabla u^{k+1} + \frac{\lambda_1^k}{r_1} \right)^2 dx dy + \frac{\delta_2}{2} \int_{\Omega} (\mathbf{p} - \mathbf{p}^k)^2 dx dy, \\ q^{k+1} &= \arg \min_q \int_{\Omega} \beta^{k+1}(x, y) |q| dx dy + \frac{r_2}{2} \int_{\Omega} \left(q - \Delta u^{k+1} + \frac{\lambda_2^k}{r_2} \right)^2 dx dy + \frac{\delta_3}{2} \int_{\Omega} (q - q^k)^2 dx dy, \\ \lambda_1^{k+1} &= \lambda_1^k + r_1 (\mathbf{p}^{k+1} - \nabla u^{k+1}), \\ \lambda_2^{k+1} &= \lambda_2^k + r_2 (q^{k+1} - \Delta u^{k+1}), \end{aligned} \right. \quad (15)$$

where $\delta_1, \delta_2, \delta_3 > 0$ are three penalty parameters and $\alpha^{k+1}(x, y)$ and $\beta^{k+1}(x, y)$ can be explicitly updated as

$$\left\{ \begin{aligned} \alpha^{k+1}(x, y) &= \left| \nabla \frac{1}{\sqrt{1 + |\nabla u^{k+1}|^2}} \right|, \\ \beta^{k+1}(x, y) &= \frac{1}{\sqrt{1 + |\nabla u^{k+1}|^2}}. \end{aligned} \right. \quad (16)$$

To solve the u -subproblem in (15), we consider its Euler-Lagrange equation, which has the form

$$\begin{aligned} \frac{u - f}{\lambda} + r_1 \operatorname{div} \left(\mathbf{p}^k - \nabla u + \frac{\lambda_1^k}{r_1} \right) \\ - r_2 \Delta \left(q^k - \Delta u + \frac{\lambda_2^k}{r_2} \right) + \delta_1 (u - u^k) = 0, \end{aligned} \quad (17)$$

namely,

$$\begin{aligned} \left(\frac{1}{\lambda} - r_1 \operatorname{div} \nabla + r_2 \Delta \Delta + \delta_1 \right) u \\ = \frac{f}{\lambda} - \operatorname{div} (r_1 \mathbf{p}^k + \lambda_1^k) + \Delta (r_2 q^k + \lambda_2^k) + \delta_1 u^k. \end{aligned} \quad (18)$$

In order to efficiently solve this nonlinear equation, we use the fast Fourier transform (FFT) with periodic boundary conditions. More concretely, u^{k+1} is given by

$$u^{k+1} = \mathcal{F}^{-1} \left[\frac{\mathcal{F} \left[f/\lambda - t \operatorname{divn}(r_1 \mathbf{p}^k + \lambda_1^k) q + h \Delta (r_2 q^k + \lambda_2^k) x + 7\delta_1 C u^k \right]}{(1/\lambda) - r_1 \mathcal{F}[\operatorname{div}\nabla] + r_2 \mathcal{F}[\Delta\Delta] + \delta_1} \right], \quad (19)$$

where \mathcal{F} is the FFT.

Both \mathbf{p} and q subproblems have closed form solutions. Specifically, the solutions of \mathbf{p} -subproblem and q -subproblem are given by the shrinkage operator:

$$\mathbf{p}^{k+1} = \operatorname{shrinkage} \left(\frac{r_1 (\nabla u^{k+1} - (\lambda_1^k / r_1)) + \delta_2 \mathbf{p}^k}{r_1 + \delta_2}, \frac{\alpha^{k+1}(x, y)}{r_1 + \delta_2} \right), \quad (20)$$

and

$$q^{k+1} = \operatorname{shrinkage} \left(\frac{r_2 (\Delta u^{k+1} - (\lambda_2^k / r_2)) + \delta_3 q^k}{r_2 + \delta_3}, \frac{\beta^{k+1}(x, y)}{r_2 + \delta_3} \right), \quad (21)$$

where $\operatorname{shrinkage}(s, \gamma) = \max\{|s| - \gamma, 0\} \circ \operatorname{sgn}(s)$. Here, \circ denotes the component-wise multiplication.

We summarize the overall algorithm for solving the spatially adaptive relaxation model (10) in Algorithm 1.

3.2. Convergence Analysis. In this subsection, we give a convergence theory for the proposed algorithm (Algorithm 1) under the assumption that a solution of the proposed model (10) exists.

Theorem 3. Assume that $\{(u^k, \mathbf{p}^k, q^k, \lambda_1^k, \lambda_2^k)\}_{k \in \mathbb{N}}$ is a sequence generated by Algorithm 1 and $\bar{u}, \bar{\mathbf{p}}, \bar{q}, \bar{\lambda}_1$, and $\bar{\lambda}_2$ are the points satisfying the following first-order optimality conditions:

$$\begin{cases} \frac{(u - f)}{\lambda} + \nabla \cdot \lambda_1 - \Delta \lambda_2 = 0, \\ \alpha(x, y) \mathbf{g} + \lambda_1 = 0, \mathbf{g} \in \partial|p| \text{ and } \alpha(x, y) = \left| \nabla \frac{1}{\sqrt{1 + |\nabla u|^2}} \right|, \\ \beta(x, y) h + \lambda_2 = 0, h \in \partial|q| \text{ and } \beta(x, y) = \frac{1}{\sqrt{1 + |\nabla u|^2}}, \\ p - \nabla u = 0, \\ q - \Delta u = 0. \end{cases} \quad (22)$$

Let $u_e^k = u^k - \bar{u}$, $\mathbf{p}_e^k = \mathbf{p}^k - \bar{\mathbf{p}}$, $q_e^k = q^k - \bar{q}$, $\lambda_{1e}^k = \lambda_1^k - \bar{\lambda}_1$, and $\lambda_{2e}^k = \lambda_2^k - \bar{\lambda}_2$ be the error sequences. If for any $\mathbf{g}^k \in \partial|p^k|$, $\bar{\mathbf{g}} \in \partial|\bar{p}|$, and $h^k \in \partial|q^k|$, $\bar{h} \in \partial|\bar{q}|$,

$$\begin{cases} \Delta_1^k := \langle (\alpha^k(x, y) - \bar{\alpha}(x, y)) \mathbf{g}^k, \mathbf{p}^k - \bar{\mathbf{p}} \rangle, \bar{\alpha}(x, y) = \left| \nabla \frac{1}{\sqrt{1 + |\nabla \bar{u}|^2}} \right|, \\ \Delta_2^k := \langle (\beta^k(x, y) - \bar{\beta}(x, y)) h^k, q^k - \bar{q} \rangle, \bar{\beta}(x, y) = \frac{1}{\sqrt{1 + |\nabla \bar{u}|^2}}, \end{cases} \quad (23)$$

are nonnegative. Then, the generated sequence $\{(u^k, \mathbf{p}^k, q^k, \lambda_1^k, \lambda_2^k)\}_{k \in \mathbb{N}}$ converges to a limit point $(u^*, \mathbf{p}^*, q^*, \lambda_1^*, \lambda_2^*)$ which satisfies the first-order optimality conditions (22).

Our proposed model (10) can be seen as a variation of the previous model in [8]. Specifically, the operator ∇^2 in (3) is changed to Δ . Furthermore, an ADMM-based algorithm same to [8] is applied to solve the proposed model (10). Therefore, the rigorous convergence proof of Algorithm 1 can refer to the proof presented in [8].

3.3. Complexity Analysis. In the following, we will give some simple analysis of complexity for the proposed method.

For our proposed method, the cost of updating u^k is $4N \log N + 26N + 1$ at each iteration, where $N = mn$ is the total number of grid points. If a root operation is equal to 12 times addition or subtraction or multiplication or division, at each iteration it will spend $61N$ ($3N$ times root operations), $11N$, $6N$, and $3N$ operations on updating \mathbf{p}^k , q^k , λ_1^k , and λ_2^k , respectively. Therefore, the total cost of one step is $4N \log N + 107N + 1$, which gives rise to the $O(N \log N)$ complexity.

4. Numerical Experiments

In this section, we give some experimental results for the proposed model (10) in terms of our proposed algorithm. For simplicity of presentation, we call it SATVL in the following. We

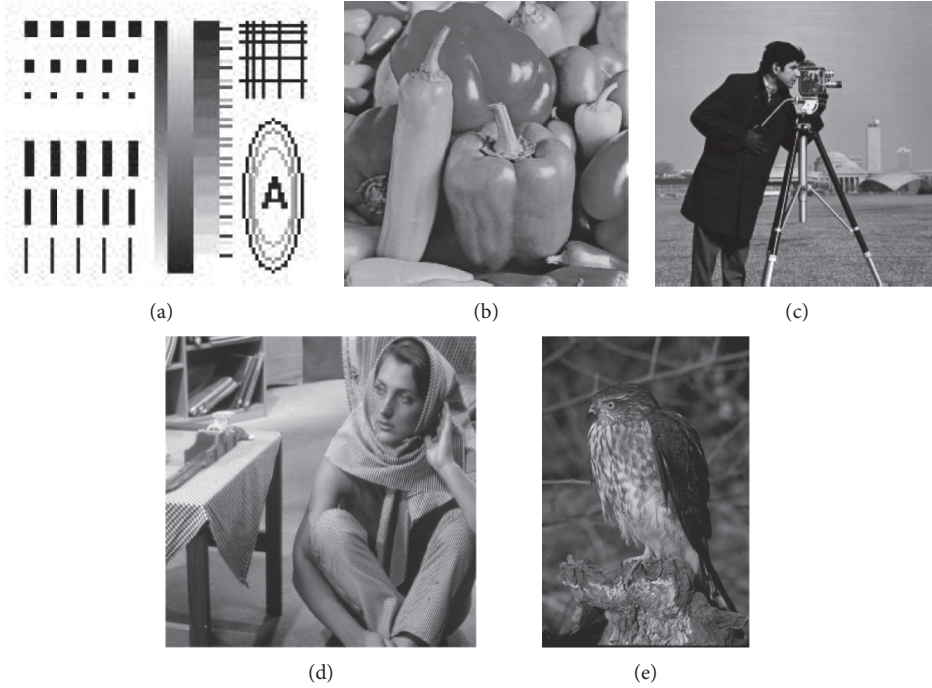


FIGURE 1: Test images of (a) shape, (b) peppers, (c) cameraman, (d) Barbara, and (e) owl.

Step 1. Input λ, r_1 , and r_2 . Initialization: $u^0 = f, \mathbf{p}^0 = 0, q^0 = 0, \lambda_1^0 = 0$, and $\lambda_2^0 = 0$. Let $k := 0$.
Step 2. Compute u^{k+1} by (19).
Step 3. Update $(\alpha^{k+1}(x, y), \beta^{k+1}(x, y))$ using u^{k+1} according to (16).
Step 4. Compute \mathbf{p}^{k+1} by (20).
Step 5. Compute q^{k+1} by (21).
Step 6. Update $(\lambda_1^{k+1}, \lambda_2^{k+1})$ by the last two equations of (15).
Step 7. Stop if the stopping criterion is satisfied. Otherwise, let $k := k + 1$, and go to Step 2.

ALGORITHM 1: (ADMM for solving (10)).

will compare our results with those of the previous algorithm for solving the spatially adaptive TV and high-order TV regularization model (3), which we call SATVTV². It should be noted that the authors in [8] proposed the same ADMM for solving model (3). All numerical experiments are conducted in MATLAB environment on a PC with a 3.85 GHz CPU processor. To assess the denoising performance qualitatively, the peak signal to noise ratio (PSNR) and the structural similarity (SSIM) [40] are adopted. Their definitions are expressed as

$$\text{PSNR} = 10 \log_{10} \frac{255^2}{(1/MN) \sum_{i=1}^M \sum_{j=1}^N (u_{i,j} - I_{i,j})^2}, \quad (24)$$

$$\text{SSIM} = \frac{(2\mu_I \mu_u + c_1)(2\sigma_{Iu} + c_2)}{(\mu_I^2 + \mu_u^2 + c_1)(\sigma_I^2 + \sigma_u^2 + c_2)},$$

where I and u represent the original clear image and the restored image, respectively, μ_I and μ_u denote the local mean values of images I and u , σ_I and σ_u express the standard deviations, σ_{Iu} signifies the covariance value between I and u , and c_1 and c_2 are two constants which can avoid near-zero

denominator values. In general, higher PSNR and SSIM values signify better performance in image denoising.

The relative error of the solution u^k is defined by

$$R(u^k) = \frac{\|u^k - u^{k-1}\|_1}{\|u^{k-1}\|_1}. \quad (25)$$

It can give some important information about the convergence of iterations. Therefore, we track its value during iteration process. In experiments, the stopping criterion is $R(u^k) \leq 5 \times 10^{-5}$ or the iteration reaches 500.

The test images are shown in Figure 1, which includes one synthetic and four natural images. Since the proximal terms are added for convergence analysis, we set $\delta_1 = \delta_2 = \delta_3 = 0$.

The values of parameters significantly affect the convergence rates and other characteristics of the methods. In our experiments, we study the influence of parameters λ, r_1 , and r_2 on the SATVTV². Concretely speaking, after taking a reasonable guess for the parameters: r_1 and r_2 , we consider different values of λ . We observe which value of λ

TABLE 1: Numerical results.

Image	Index	$\sigma = 10$		$\sigma = 20$		$\sigma = 30$	
		SATVTV ²	SATVL	SATVTV ²	SATVL	SATVTV ²	SATVL
Shape 128×128	PSNR	34.188	34.017	29.186	28.856	25.777	25.536
	SSIM	0.988	0.986	0.976	0.971	0.959	0.954
	Iter.	500	500	500	500	500	500
	CPU (s)	21.562	11.562	20.234	11.343	19.421	12.500
Peppers 256×256	PSNR	33.355	33.098	29.428	29.152	27.081	26.768
	SSIM	0.959	0.956	0.921	0.914	0.885	0.874
	Iter.	203	329	410	500	500	500
	CPU (s)	21.218	20.031	42.406	28.265	46.593	28.250
Cameraman 256×256	PSNR	33.117	32.823	29.025	28.838	27.248	26.961
	SSIM	0.954	0.949	0.903	0.899	0.873	0.863
	Iter.	205	376	283	500	367	500
	CPU (s)	25.078	22.375	29.234	27.500	37.593	26.875
Barbara 512×512	PSNR	31.898	31.559	27.197	26.858	24.672	24.557
	SSIM	0.943	0.936	0.860	0.841	0.768	0.761
	Iter.	272	349	490	500	500	500
	CPU (s)	145.984	140.890	271.546	195.187	280.484	203.578
Owl 321×481	PSNR	33.375	33.096	29.600	29.378	27.685	27.498
	SSIM	0.952	0.947	0.895	0.888	0.848	0.841
	Iter.	379	461	500	500	500	500
	CPU (s)	104.936	89.436	140.686	92.030	140.530	92.751

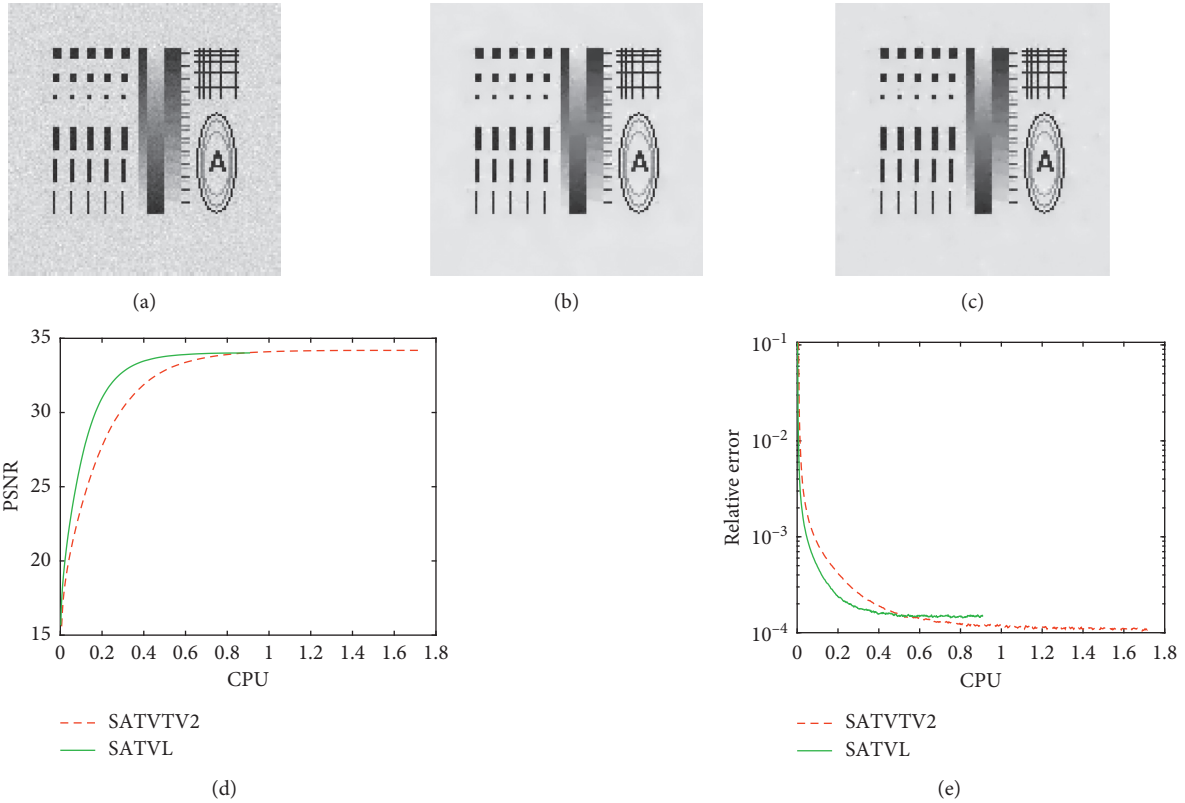


FIGURE 2: (a) Noisy shape image with $\sigma = 10$; (b, c) restored shape images by SATVTV² and SATVL, respectively; (d, e) the plots of PSNR and relative error versus CPU time, respectively.

could contribute to the biggest value of PSNR, and then we set it to be the value of λ . And in turn, we use the same strategy for the choice of other parameters. Similar strategy

is adopted for tuning the parameters of our SATVL. For the parameter tuning, the algorithms are terminated after the stopping criterion is satisfied.

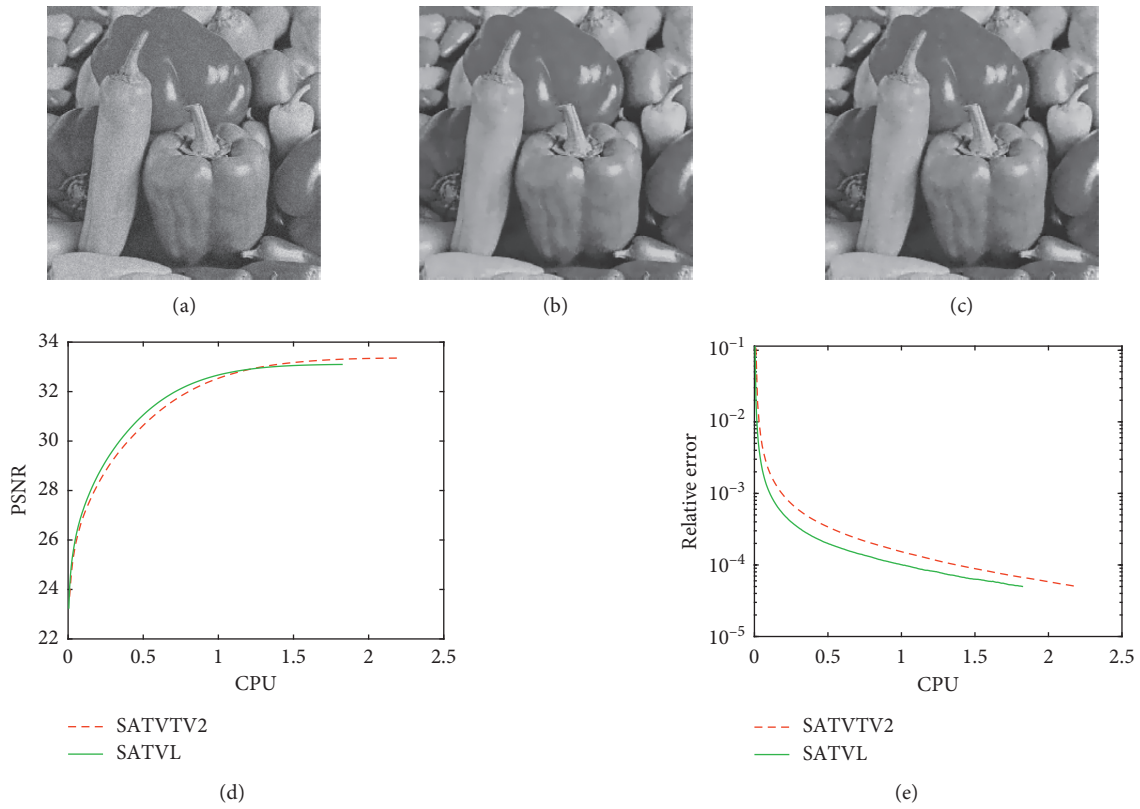


FIGURE 3: (a) Noisy pepper image with $\sigma = 10$; (b, c) restored pepper images by SATVTV2 and SATVL, respectively; (d, e) the plots of PSNR and relative error versus CPU time, respectively.

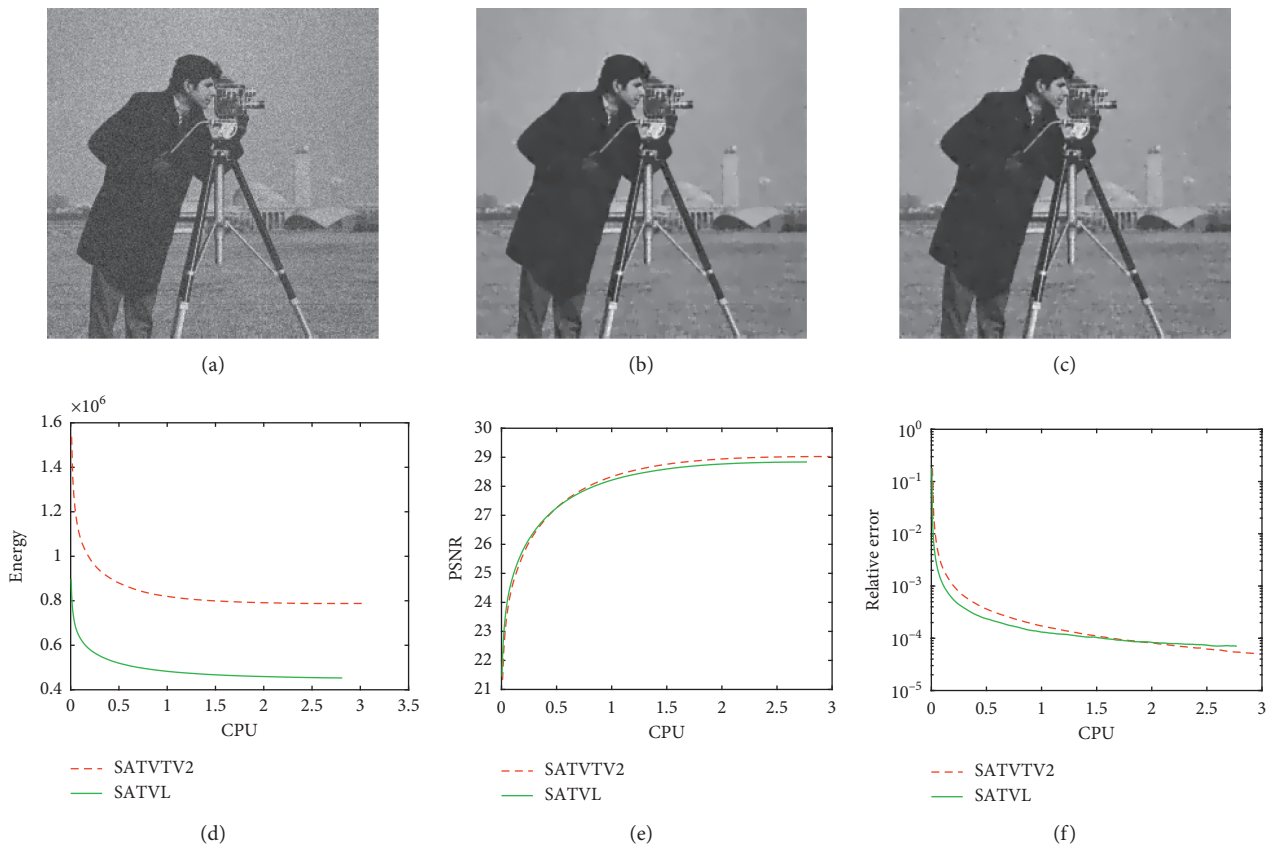


FIGURE 4: (a) Noisy cameraman image with $\sigma = 20$; (b, c) restored cameraman images by SATVTV2 and SATVL, respectively; and (d-f) the plots of energy, PSNR, and relative error versus CPU time, respectively.

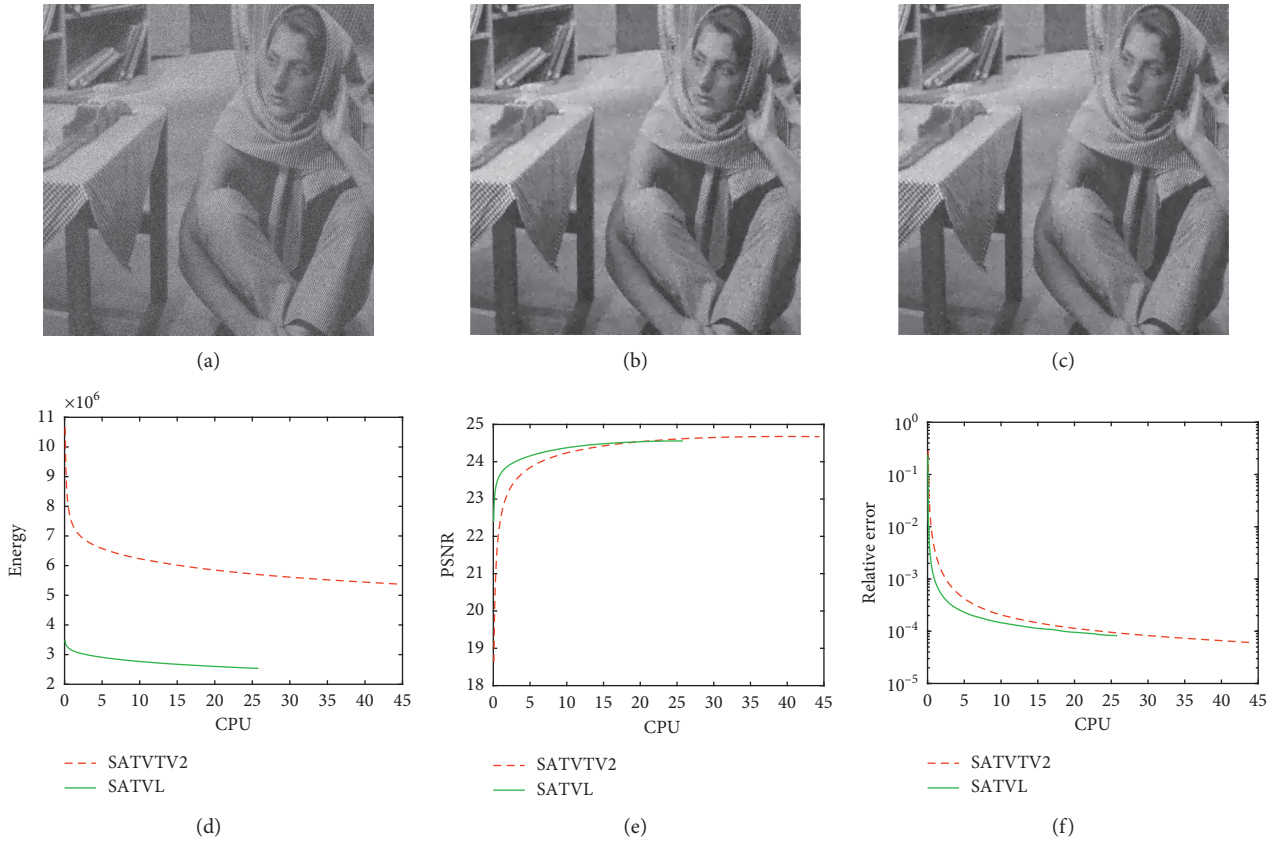


FIGURE 5: (a) Noisy Barbara image with $\sigma = 30$; (b, c) restored Barbara images by SATVTV² and SATVL, respectively; and (d–f) the plots of energy, PSNR, and relative error versus CPU time, respectively.

Experiment 1. In this example, we use the shape image as the test image. We first consider to restore the image corrupted by Gaussian white noise with $\sigma = 10$. For the SATVTV², we set $\lambda = 7.4$, $r_1 = 0.11$, and $r_2 = 0.35$. For our SATVL, we use $\lambda = 12$, $r_1 = 0.03$, and $r_2 = 0.25$. Besides, the Gaussian white noises at levels $\sigma = 20$ and $\sigma = 30$ are added for comparison, respectively. The numerical results are arranged in Table 1, while the corresponding visual results for noise level $\sigma = 10$ are shown in Figure 2. In Table 1, Iter. and CPU (s) denote the number of iterations and the CPU time in seconds required for the whole denoising process.

Experiment 2. In our second example, the pepper image is adopted as the test image. The original image is degraded by Gaussian white noise with $\sigma = 10$. The parameters are set to be $\lambda = 9$, $r_1 = 0.005$, and $r_2 = 0.7$ for the SATVTV² and $\lambda = 14.5$, $r_1 = 0.001$, and $r_2 = 0.7$ for the SATVL. Then, we consider more Gaussian noises at $\sigma = 20$ and $\sigma = 30$, respectively. Here, the values of parameters need to be reset. Numerical results are also listed in Table 1. The visual results about noise level $\sigma = 10$ are presented in Figure 3.

Experiment 3. In our third example, we test the cameraman image. The original image is corrupted by Gaussian white noise with $\sigma = 10$. Here, parameters for the SATVTV² and our SATVL are set to be $\lambda = 7.2$, $r_1 = 0.008$, and $r_2 = 0.67$ and $\lambda = 12.4$, $r_1 = 0.002$, and $r_2 = 0.71$, respectively. In

order to show better visual results, we also test the cases of noise levels $\sigma = 20$ and $\sigma = 30$. Results of this experiment are given in Table 1. The visual results about the noise level $\sigma = 20$ are presented in Figure 4.

Experiment 4. In this example, we choose the Barbara image. Same to the above three experiments, we test the noisy images with different noise levels. Related numerical results are reported in Table 1, and the visual results about the noise level $\sigma = 30$ are displayed in Figure 5.

Experiment 5. In the last example, the owl image is used. To show the advantage of our proposed method, we also test noisy images with three different noise levels. For each algorithms, related parameters have been tuned to obtain the best restoration performance uniformly.

In terms of PSNR and SSIM, the denoising results by these two methods are similar. It is easy to see from Figures 2–5 that the visual results of the SATVL are comparable to the SATVTV². As shown in Table 1, our SATVL is faster than the SATVTV². Experiments have shown this situation at different noise levels. From the plots of PSNR and relative error versus CPU time in Figures 2–5, we can also draw this conclusion. Besides, it is shown from these plots that the SATVL has converged, just as the SATVTV² did. Actually, it is clear that the energy and PSNR have converged to a steady state.

5. Conclusion

In this paper, we have proposed a new relaxation model based on mean curvature for adaptive image denoising. We analyzed the connections to the existing models. Furthermore, we proposed an efficient ADMM to solve the proposed relaxation model and studied its convergence and complexity. Compared with the previous method for an adaptive first- and second-order regularization-based image denoising model, experimental results show that our proposed method is fast. Obviously, the proposed regularization term can be applied to other image processing problems, such as image deblurring, and image segmentation.

Data Availability

The data used to support the findings of this study are available from the corresponding author upon request.

Conflicts of Interest

The authors declare that they have no conflicts of interest.

Acknowledgments

This work was supported by the Science and Technology Project of Jiangxi Provincial Department of Education (GJJ171015), the Science Foundation for Post Doctorate of China (2020M672484), the Natural Science Foundation of Jiangxi Province (20192BAB211005 and 20192BAB217003), and the NNSF of China (61865012 and 61861032).

References

- [1] R. W. Liu, L. Shi, W. Huang, J. Xu, S. C. H. Yu, and D. Wang, "Generalized total variation-based MRI Rician denoising model with spatially adaptive regularization parameters," *Magnetic Resonance Imaging*, vol. 32, no. 6, pp. 702–720, 2014.
- [2] L. I. Rudin, S. Osher, and E. Fatemi, "Nonlinear total variation based noise removal algorithms," *Physica D: Nonlinear Phenomena*, vol. 60, no. 1–4, pp. 259–268, 1992.
- [3] J. Zhang and Y.-F. Yang, "Nonlinear multigrid method for solving the anisotropic image denoising models," *Numerical Algorithms*, vol. 63, no. 2, pp. 291–315, 2013.
- [4] X. Zhang, M. Burger, X. Bresson, and S. Osher, "Bregmanized nonlocal regularization for deconvolution and sparse reconstruction," *SIAM Journal on Imaging Sciences*, vol. 3, no. 3, pp. 253–276, 2010.
- [5] T. Liu, Z. Chen, S. Liu, Z. Zhang, and J. Shu, "Blind image restoration with sparse priori regularization for passive millimeter-wave images," *Journal of Visual Communication and Image Representation*, vol. 40, pp. 58–66, 2016.
- [6] J. Zhang, R. Chen, C. Deng, and S. Wang, "Fast linearized augmented Lagrangian method for Euler's elastica model," *Numerical Mathematics: Theory, Methods and Applications*, vol. 10, no. 1, pp. 98–115, 2017.
- [7] J. Zhang and Y.-F. Yang, "Nonlinear multigrid method for solving the LLT model," *Applied Mathematics and Computation*, vol. 219, no. 10, pp. 4964–4976, 2013.
- [8] Q. Zhong, R. W. Liu, and Y. Duan, "Spatially adapted first and second order regularization for image reconstruction: from an image surface perspective," 2019, <https://arxiv.org/abs/1912.00628>.
- [9] W. Zhu and T. Chan, "Image denoising using mean curvature of image surface," *SIAM Journal on Imaging Sciences*, vol. 5, no. 1, pp. 1–32, 2012.
- [10] M. R. Chowdhury, J. Zhang, J. Qin, and Y. Lou, "Poisson image denoising based on fractional-order total variation," *Inverse Problems and Imaging*, vol. 14, no. 1, pp. 77–96, 2020.
- [11] J. Zhang, Z. Wei, and L. Xiao, "Adaptive fractional-order multi-scale method for image denoising," *Journal of Mathematical Imaging and Vision*, vol. 43, no. 1, pp. 39–49, 2012.
- [12] A. Chambolle, "An algorithm for total variation minimization and applications," *Journal of Mathematical Imaging and Vision*, vol. 20, pp. 89–97, 2004.
- [13] T. F. Chan, G. H. Golub, and P. Mulet, "A nonlinear primal-dual method for total variation-based image restoration," *SIAM Journal on Scientific Computing*, vol. 20, no. 6, pp. 1964–1977, 1999.
- [14] T. Goldstein and S. Osher, "The split Bregman method for L1-regularized problems," *SIAM Journal on Imaging Sciences*, vol. 2, no. 2, pp. 323–343, 2009.
- [15] X. C. Tai and C. Wu, "Augmented Lagrangian method, dual methods and split Bregman iteration for ROF model," in *Proceedings of the SSVN*, Voss, Norway, June 2009.
- [16] C. Wu and X.-C. Tai, "Augmented Lagrangian method, dual methods, and split Bregman iteration for ROF, vectorial TV, and high order models," *SIAM Journal on Imaging Sciences*, vol. 3, no. 3, p. 300, 2010.
- [17] Y. Wang, W. Yin, and Y. Zhang, *A Fast Algorithm for Image Deblurring with Total Variation Regularization*, Rice University, Houston, TX, USA, 2007.
- [18] C. A. Micchelli, L. Shen, and Y. Xu, "Proximity algorithms for image models: denoising," *Inverse Problems*, vol. 27, p. 30, 2011.
- [19] H. Chang, X. Zhang, X.-C. Tai, and D. Yang, "Domain decomposition methods for nonlocal total variation image restoration," *Journal of Scientific Computing*, vol. 60, no. 1, pp. 79–100, 2014.
- [20] R. W. Liu, D. Wu, C. S. Wu, T. Xu, and N. Xiong, "Constrained nonconvex hybrid variational model for edge-preserving image restoration," in *Proceedings of the 2015 IEEE International Conference on Systems, Man, and Cybernetics*, pp. 1809–1814, Kowloon, China, October 2015.
- [21] W. Lu, J. Duan, Z. Qiu, Z. Pan, R. W. Liu, and L. Bai, "Implementation of high-order variational models made easy for image processing," *Mathematical Methods in the Applied Sciences*, vol. 39, no. 14, pp. 4208–4233, 2016.
- [22] Y. Gong, "Mean curvature is a good regularization for image processing," *IEEE Transactions on Circuits and Systems for Video Technology*, vol. 29, no. 8, pp. 2205–2214, 2019.
- [23] Y. Duan, Y. Wang, and J. Hahn, "A fast augmented Lagrangian method for Euler's elastica models," *Numerical Mathematics: Theory, Methods and Applications*, vol. 6, no. 1, pp. 47–71, 2013.
- [24] T. Ringholm, J. Lazić, and C.-B. Schönlieb, "Variational image regularization with Euler's elastica using a discrete gradient scheme," *SIAM Journal on Imaging Sciences*, vol. 11, no. 4, pp. 2665–2691, 2018.
- [25] X.-C. Tai, J. Hahn, and G. J. Chung, "A fast algorithm for Euler's elastica model using augmented Lagrangian method," *SIAM Journal on Imaging Sciences*, vol. 4, no. 1, pp. 313–344, 2011.
- [26] D. N. H. Thanh, V. B. S. Prasath, S. Dvoenko, and L. M. Hieu, "An adaptive image inpainting method based on Euler's elastica with adaptive parameters estimation and the discrete gradient method," *Signal Processing*, vol. 178, Article ID 107797, 2021.

- [27] M. Yashtini and S. H. Kang, "A fast relaxed normal two split method and an effective weighted TV approach for Euler's elastica image inpainting," *SIAM Journal on Imaging Sciences*, vol. 9, no. 4, pp. 1552–1581, 2016.
- [28] W. Zhu, X. C. Tai, X.-C. Tai, and T. Chan, "Augmented Lagrangian method for a mean curvature based image denoising model," *Inverse Problems & Imaging*, vol. 7, no. 4, pp. 1409–1432, 2013.
- [29] W. Zhu, X.-C. Tai, and T. Chan, "A fast algorithm for a mean curvature based image denoising model using augmented Lagrangian method," *Efficient Algorithms for Global Optimization Methods in Computer Vision*, vol. 8293, pp. 104–118, 2014.
- [30] J. Zhang, C. Deng, Y. Shi, S. Wang, and Y. Zhu, "A fast linearised augmented Lagrangian method for a mean curvature based model," *East Asian Journal on Applied Mathematics*, vol. 8, no. 3, pp. 463–476, 2018.
- [31] D. N. H. Thanh, V. B. S. Prasath, L. M. Hieu, and S. Dvoenko, "An adaptive method for image restoration based on high-order total variation and inverse gradient," *Signal, Image and Video Processing*, vol. 14, no. 6, pp. 1189–1197, 2020.
- [32] P.-W. Hsieh, P.-C. Shao, and S.-Y. Yang, "A regularization model with adaptive diffusivity for variational image denoising," *Signal Processing*, vol. 149, pp. 214–228, 2018.
- [33] Z.-F. Pang, H.-L. Zhang, S. Luo, and T. Zeng, "Image denoising based on the adaptive weighted TV regularization," *Signal Processing*, vol. 167, Article ID 107325, 2020.
- [34] A. Kumar, M. Omair Ahmad, and M. N. S. Swamy, "Tchebichef and adaptive steerable-based total variation model for image denoising," *IEEE Transactions on Image Processing*, vol. 28, no. 6, pp. 2921–2935, 2019.
- [35] Y. Chen, W. W. Hager, M. Yashtini, X. Ye, and H. Zhang, "Bregman operator splitting with variable stepsize for total variation image reconstruction," *Computational Optimization and Applications*, vol. 54, no. 2, pp. 317–342, 2013.
- [36] D. Hong, N. Yokoya, J. Chanussot, and X. X. Zhu, "An augmented linear mixing model to address spectral variability for hyperspectral unmixing," *IEEE Transactions on Image Processing*, vol. 28, no. 4, pp. 1923–1938, 2019.
- [37] D. Hong, N. Yokoya, N. Ge, J. Chanussot, and X. X. Zhu, "Learnable manifold alignment (LeMA): a semi-supervised cross-modality learning framework for land cover and land use classification," *ISPRS Journal of Photogrammetry and Remote Sensing*, vol. 147, pp. 193–205, 2019.
- [38] D. Hong, N. Yokoya, J. Chanussot, and X. X. Zhu, "CoSpace: common subspace learning from hyperspectral-multispectral correspondences," *IEEE Transactions on Geoscience and Remote Sensing*, vol. 57, no. 7, pp. 4349–4359, 2019.
- [39] R. H. Chan, H. Liang, S. Wei, M. Nikolova, and X. C. Tai, "High-order total variation regularization approach for axially symmetric object tomography from a single radiograph," *Inverse Problems and Imaging*, vol. 9, no. 1, pp. 55–77, 2015.
- [40] Z. Wang, A. C. Bovik, H. R. Sheikh, and E. P. Simoncelli, "Image quality assessment: from error visibility to structural similarity," *IEEE Transactions on Image Processing*, vol. 13, no. 4, pp. 600–612, 2004.